

Chaos and Carter: Extreme-mass-ratio systems of relativistic rotating black holes in astrophysical environments

Kyriakos Destounis^{1,*} and Pedro G. S. Fernandes^{2,†}

¹*CENTRA, Departamento de Física, Instituto Superior Técnico – IST,
Universidade de Lisboa – UL, Avenida Rovisco Pais 1, 1049-001 Lisboa, Portugal*

²*Institut für Theoretische Physik, Universität Heidelberg, Philosophenweg 12, 69120 Heidelberg, Germany*

Extreme-mass-ratio inspirals, where a stellar-mass object orbits a supermassive black hole, are prime sources of millihertz gravitational waves for upcoming space-based detectors. While most studies assume idealized vacuum backgrounds, realistic extreme-mass-ratio binaries are embedded in astrophysical environments, such as accretion disks, stellar clusters, or dark matter spikes, disks and halos, that can significantly alter the orbital dynamics. We explore bound geodesics around general-relativistic solutions describing rotating black holes surrounded by matter halos, for the first time, and map how environmental effects meddle with the spacetime symmetries of vacuum spinning (Kerr) black holes. In particular, we find that the loss of a Carter-like constant leads to geodesic non-integrability and the onset of chaos. This manifests through resonant island and chaotic layer formations around transient orbital resonances in phase space; features that are otherwise completely absent in integrable Kerr geodesics. Resonant islands, which are extended, non-zero volume regions in phase space, encapsulate periodic orbit points. Non-integrability ensures that the periodicity of the central resonant point is shared throughout the island’s geodesics, thus effectively enhancing the lifespan of resonances, beyond Kerr-based predictions. Therefore, they can subject distinct imprint on gravitational-wave signals, with significant consequences for gravitational-wave modeling and parameter inference of astrophysical extreme-mass-ratio inspirals.

I. INTRODUCTION

As gravitational-wave (GW) detections from ground-based interferometers are increasing exponentially [1, 2], our understanding of gravitation becomes more precise [3]. In the verge of an era where GW detections are systematically becoming far more sensitive and accurate than the initial, though still ground-breaking, detection of 2015 [4], novel space-borne detectors, like the Laser Interferometer Space Antenna (LISA) [5], will unlock a new window of the Cosmos through the detection of gravitational radiation emitted by enticing theorized sources, thus transforming our understanding of GW astrophysics and astronomy [6, 7].

The main categories of LISA targets that regard fundamental physics [8–10] and astrophysics [11, 12] alone are enthralling; supermassive black-hole (BH) mergers, such as those occurring during galactic collisions that include such cosmic giants in their very core [13, 14], compact binary systems in the Milky Way, and infalling stellar-mass compact objects into supermassive BHs, known as extreme-mass-ratio inspirals (EMRIs) [15–17]. LISA will be also sensitive to the measurement of the stochastic GW background which has an immense value for gravitation, cosmology and particle physics. LISA will contribute to the understanding of the early Universe, the nature of dark matter and dark energy, as well as potential deviations from standard cosmological models and “beyond the Standard Model” physics [18].

EMRIs are one of the most promising targets of LISA due to their expected formation rates in galactic centers [19–22], and the fact that the secondary stellar-mass companion is expected to perform thousands of revolutions in the strong-field regime before plunging into the supermassive primary. Their extremely large lifetime instantly renders numerical relativity impractical. New techniques have been used so far to speed up the process of waveform modeling in EMRIs [23–25], though there is still an abundance of phenomenology that has to be taken into account. Their unique cosmic design is tailored for precision tests of General Relativity (GR) [26–40], probing the existence of new fundamental fields [41–49], and even testing the existence of astrophysical environments around EMRIs [50–75].

Most binary merger events should, in principle, occur inside cosmogonic environments that veil the massiveness of our Universe [76–78]. In fact, astrophysical environments pose a key feature in various contexts of gravitational radiation; from the inspiral till the ringdown [79–96]. Realistic EMRIs, are, thus, expected to interact with surrounding matter. These environmental components can alter the orbital dynamics of EMRIs. We now have more than enough evidence that matter environments, luminous or otherwise, are present in the surroundings of compact objects [97–110]. Therefore, a huge effort is spent into employing systematically environmental effects in GW generation and propagation from EMRIs.

The bulk of EMRI analyses are treating environments within perturbation theory or with post-Newtonian schemes that approximate the self-gravity of matter, estimate dynamical friction, and simplify gravitational redshift or peculiar motion [111–116]. Even though successful at the time, due to the demands of LISA parameter

* kyriakosdestounis@tecnico.ulisboa.pt

† fernandes@thphys.uni-heidelberg.de

inference a growing need for first-principle calculations of BHs in astrophysical environments is inevitable. To go beyond crude estimates, a general-relativistic, exact solution of the field equations has been obtained [117], that describes a BH immersed in a Hernquist-type dark matter halo [118], and was further extended to a plethora of numerical BH solutions with different dark matter distributions around them [119–122]. The axial and polar GW fluxes of circular equatorial EMRIs including general-relativistic, static and spherically-symmetric BHs surrounded by generic environments around have been investigated in a relativistic setup [123–126]. The results strongly suggest the need for a paradigm-shifting strategy in order to accurately capture environmental effects in EMRIs.

A milestone regarding BH in environments was achieved recently; a fully-relativistic numerical configuration of a rotating BH embedded in a Hernquist-type matter halo [127]. These solutions, and the analysis of EMRIs that will be performed with them, will lead us one step closer to the ultimate goal; a generic perturbation scheme for general-relativistic BHs in astrophysical environments that handles calculations of generic EMRI fluxes. This technique will provide unlimited access to precise EMRI waveforms, and to date it only exists in spherical symmetry [96, 123]. EMRIs evolve adiabatically due to the large mass disparity between the primary and secondary. This allows to perceive the evolution of the secondary, at leading-order, as a geodesic of a massive test-particle in a fixed background. At sub-leading order, radiation reaction effects take place and lead the secondary through a drift of successively-damped geodesics.

Formally, a general, stationary and axisymmetric spacetime possesses two Killing vector fields associated with stationarity and axisymmetry. These Killing vector fields are associated with two constants (integrals) of motion; the conserved energy and azimuthal angular momentum. Vacuum Kerr spacetimes have the privilege of possessing yet another constant of motion, namely the Carter constant [128], which is associated to a rank-two Killing tensor field. The conservation of the energy, azimuthal angular momentum and Carter constant of the test particle, are enough to deem the geodesics separable, i.e., *integrable*. This results to four, decoupled, first-order ordinary differential equations for the degrees of freedom of the metric [129].

On the other hand, if the, very fragile, Carter symmetry is broken, then even though the temporal and azimuthal geodesics still form decoupled and first-order differential equations, the radial and polar motion of geodesics pose a coupled second-order dynamical system. In this case, the geodesics of spacetime are *non-integrable*, i.e. they lack a separation constant, and chaotic phenomenology in the orbital phase space emanates [129]. These phenomena appear in many distinctive ways in various dynamical systems. The most relevant indicator of chaos in EMRIs is the formation of a Birkhoff chain around a resonant point in a Poincaré surface of section.

The chain includes nested island formations around the periodic stable points, also known as resonant islands.

Resonances in Kerr EMRIs are by themselves challenging for GW modeling and data analysis [130]. This is due to the fact that when the secondary crosses a Kerr resonance, it undergoes a transient phase from a quasi-periodic to periodic orbit and back that can last up to dozens of cycles [131–134]. If the geodesics are non-integrable, the resonant islands that surround stable periodic points become regions of shared periodicity for all geodesics that occupy the island. This inevitably leads to resonances that last much longer [135–138] (\sim hundreds of orbits of purely resonant motion) and designates the existence of non-integrability and indirect chaos.

Astrophysical chaos has proven to be a prominent effect in non-Kerr EMRIs, that can significantly affect the GW frequency evolution when a resonant island is crossed. The studies conducted so far have employed theory-agnostic primaries that are tailored to break integrability [139–141], pathological solutions of GR [142–144], exotic compact object primaries [145, 146], and even EMRI analogs [147, 148]. Even though the above classes of EMRIs discussed might lead to chaotic phenomena both at the orbital and GW level, they are either exotic, arise from modifications of gravity or include secondary effects that modify the geodesic equations.

In this work, we embark into a tentative geodesic treatment of general-relativistic solutions of the field equations, describing rotating BHs surrounded by a Hernquist-type dark matter distribution [127], in an attempt to examine if there are imprints of non-integrability when, relativistically-constructed¹, rotating BHs in environments are present. This analysis results to a novel class of chaos that is environmentally-driven and purely relativistic. Thus here, we lay the groundwork for future EMRI studies, that will include radiation reaction, and provides powerful insights into how realistic astrophysical environments influence spacetime symmetries.

II. BLACK HOLES IN ASTROPHYSICAL ENVIRONMENTS

In what follows, we review the first exact, fully-relativistic, solution to the field equations that describes a static and spherically-symmetric BH in the center of a matter halo environment² [117]. Afterwards, we re-

¹ Very early attempts for unraveling chaotic phenomena in Schwarzschild BHs *perturbed* with matter halos, that are introduced in the form of dipolar, quadrupolar and octopolar perturbations to background have been successful, though the contribution of the matter halos was added by hand to vacuum GR backgrounds and introduced various pathologies [149, 150].

² Of course, other general-relativistic solutions exist but they do not include a halo of matter but rather a thin disk around the BH, see e.g. [151–153].

visit the generalization of this exact solution to a general-relativistic and fully-numerical spacetime that describes a stationary and axially-symmetric rotating BH surrounded by an environment [127].

A. Exact, static and spherically-symmetric BHs in matter halos

The first, exact solution of Einstein's equations that describes a static and spherically-symmetric BH placed in the core of a dark matter halo was obtained in [117]. The basic principle of the construction of the environment is the assumption of many gravitating masses, that follow all possible spherical geodesics around a central point where the BH exists, thus building an Einstein cluster [121, 154–169]. By integrating all geodesics over a finite radius range leads to introducing an anisotropic fluid with zero radial pressure (since the Einstein cluster assumes geodesics) and non-zero tangential pressure P_t that drives the fluid, such that

$$T_\nu^\mu = \text{diag}(-\varepsilon, 0, P_t, P_t), \quad (1)$$

where ε is the energy density of the matter profile. Even though in [117] a density profile was used that describes dark matter halos around galaxies [170–173], namely the Hernquist density profile [118]

$$\varepsilon = \frac{M_{\text{halo}} a_0}{2\pi r(r + a_0)^3}, \quad (2)$$

where M_{halo} is the mass of the halo, a_0 its length scale and M_{halo}/a_0 defines the halo compactness, there have been other configurations that have been constructed in an equivalent manner though they do not lead to an exact, but rather a numerical solution. The assumption of spherical symmetry, together with a Hernquist-inspired matter distribution

$$m(r) = M_{\text{BH}} + \frac{M_{\text{halo}} r^2}{(a_0 + r)^2} \left(1 - \frac{2M_{\text{BH}}}{r}\right)^2, \quad (3)$$

where M_{BH} is the mass of the primary central BH, leads to the geometry³

$$ds^2 = -f(r)dt^2 + \frac{dr^2}{1 - 2m(r)/r} + r^2 d\Omega^2, \quad (4)$$

³ Recently, it was shown in Ref. [169] that this, and other geometries following from the Einstein cluster construction, are also solutions to a particular vector-tensor theory, where the vector encodes the astrophysical environment.

with

$$f(r) = \left(1 - \frac{2M_{\text{BH}}}{r}\right) e^\Upsilon, \quad (5)$$

$$\Upsilon = -\pi\sqrt{M_{\text{halo}}/\xi} + 2\sqrt{M_{\text{halo}}/\xi} \arctan \left[\frac{r + a_0 - M_{\text{halo}}}{\sqrt{M_{\text{halo}}\xi}} \right], \quad (6)$$

$$\xi = 2a_0 - M_{\text{halo}} + 4M_{\text{BH}}. \quad (7)$$

At small scales, Eq. (4) describes a BH of mass M_{BH} , while at large scales the Newtonian potential corresponds to that of the Hernquist profile (2), dominated by the halo's mass M_{halo} . The spacetime consists of a BH event horizon at $r = r_h = 2M_{\text{BH}}$, a curvature singularity at $r = 0$, while the configurations has Arnowitt-Deser-Misner (ADM) mass equal to $M_{\text{ADM}} = M_{\text{halo}} + M_{\text{BH}}$. For galactic dark matter halos, the inequality $M_{\text{BH}} \ll M_{\text{halo}} \ll a_0$ must hold while the compactness should satisfy the inequality $M_{\text{halo}}/a_0 \lesssim 10^{-4}$ [172], in order to describe the dark matter halo of a galaxy. Even so, in the context of BH environments, the compactness, in principle, can be treated as a parameter of spacetime as long as $M_{\text{halo}} < 2(a_0 + 2M_{\text{BH}})$, in order to avoid spacetime ambiguities.

B. Including spin: general-relativistic, rotating BHs in matter halos

Astrophysical BHs are generally expected to rotate and to reside in galaxies that themselves possess intrinsic angular momentum. Incorporating rotation into the models discussed in the previous section is therefore crucial for a complete understanding of how environments influence astrophysical BHs, and one must go beyond spherical symmetry. However, the absence of spherical symmetry appears to rule out the possibility of obtaining closed-form analytic solutions.

Using numerical methods, Ref. [127] has recently obtained stationary and axisymmetric solutions to the Einstein equations, describing rotating BHs immersed in an astrophysical environment. In the following, we describe briefly the formalism and the numerical method used in Ref. [127], to which the reader is referred to for a more detailed discussion.

We consider solutions to the Einstein field equations, $G_{\mu\nu} = 8\pi T_{\mu\nu}$, sourced by an anisotropic fluid, with stress-energy tensor

$$T_{\mu\nu} = (\varepsilon + p_1) u_\mu u_\nu + p_1 g_{\mu\nu} + (p_r - p_1) k_\mu k_\nu + (p_2 - p_1) s_\mu s_\nu, \quad (8)$$

where ε , p_r , p_1 and p_2 are the energy density, radial pressure and transverse pressures in the comoving frame of the fluid, respectively. The vectors u^μ , k^μ and s^μ are, respectively, the four-velocity of the fluid and spacelike vectors that define the directions of anisotropy such that

$u^\mu u_\mu = -1$, $k^\mu k_\mu = 1$, $s^\mu s_\mu = 1$, $u^\mu k_\mu = 0$, $u^\mu s_\mu = 0$, and $k^\mu s_\mu = 0$.

We use a metric that is stationary, axially-symmetric and circular, in quasi-isotropic coordinates, described by four functions, f , g , h , ω , of r and θ

$$ds^2 = -f \frac{N_-^2}{N_+^2} dt^2 + \frac{g}{f} N_+^4 \left[h (dr^2 + r^2 d\theta^2) + r^2 \sin^2 \theta (d\varphi - \omega dt)^2 \right], \quad (9)$$

where $N_\pm = (1 \pm r_h/r)$. In these coordinates, the four-velocity of the fluid is

$$u^\mu = \frac{1}{\sqrt{-(g_{tt} + 2\Omega g_{t\varphi} + \Omega^2 g_{\varphi\varphi})}} (1, 0, 0, \Omega), \quad (10)$$

where $\Omega \equiv \Omega(r, \theta)$ is the angular velocity of the fluid. Following Ref. [127] we focus on the simplest case, where $\Omega = \omega$, such that the angular velocity of the dark matter halo is the frame-dragging angular velocity.

The total mass of the spacetime obeys $M_{\text{ADM}} = M_{\text{BH}} + M_{\text{halo}}$, where $M_{\text{BH}} = \frac{\kappa}{4\pi} A_h + 2\Omega_h J_h$, is the mass of the BH⁴, and M_{halo} is the mass of the halo. The total mass M_{ADM} and angular momentum J_h ⁵ can also be computed from the asymptotic decay of the metric components $g_{tt} = -1 + 2M_{\text{ADM}}/r + \mathcal{O}(r^{-2})$, and $g_{t\varphi} = -2J_h \sin^2 \theta / r + \mathcal{O}(r^{-2})$, while the surface gravity and the area of the event horizon for the metric (9) are computed as

$$\kappa = \frac{f}{8r_h \sqrt{gh}}, \quad A_h = 32\pi r_h^2 \int_0^\pi \frac{g\sqrt{h}}{f} \sin \theta d\theta, \quad (11)$$

where these expressions are to be evaluated at $r = r_h$.

To solve the field equations and obtain stationary, axially-symmetric BH solutions, we use the six independent combinations of equations that follow from the Einstein equations (see Ref. [127]). The system, however, contains eight undetermined functions of r and θ , the four metric functions and the four eigenvalues of the stress-energy tensor. The field equations, can only determine six of these functions, that we choose as the four metric functions and the two tangential pressures p_1 and p_2 . To close the system we choose, from physical considerations, a profile for the energy density ε of the dark matter halo, and provide an equation of state for p_r , namely, $p_r = 0$, in accordance with the Einstein cluster. Motivated by the Hernquist profile, and by Ref. [117], we use following profile for the energy density

$$\varepsilon = \frac{\mathcal{M} (a_0 + r_h)}{2\pi r (r + a_0)^3} \left(1 - \frac{r_h}{r} \right)^2 b^{-5}, \quad (12)$$

⁴ The quantities κ , A_h , Ω_h and J_h are, respectively, the surface gravity, horizon area of the BH, angular velocity of the horizon, and the angular momentum of the BH.

⁵ Since $\Omega = \omega$, the total angular momentum is equal to the angular momentum of the black hole.

where \mathcal{M} and a_0 are parameters, and $b \equiv b(r)$ is a complicated function of r presented in Ref. [127]. While a_0 represents a typical length scale associated with the halo, the parameter \mathcal{M} represents, to leading order in an expansion in powers of \mathcal{M}/a_0 , the mass of the halo M_{halo} . The function $b(r)$ guarantees that the parameters \mathcal{M} and a_0 have suitable physical meaning. Importantly, $b > 0$, and therefore $\varepsilon \geq 0$. In the large r limit, this profile for ε agrees with the Hernquist profile, up to terms proportional to r_h .

The functions obey the following boundary conditions. At the horizon ($r = r_h$) we have $\partial_r f = \partial_r g = \partial_r h = \partial_r p_1 = \partial_r p_2 = 0$, $\omega = \Omega_h$, while asymptotically they obey $f = g = h = 1$, $\omega = p_1 = p_2 = 0$. Regularity, axial symmetry and parity considerations imply $\partial_\theta f = \partial_\theta g = \partial_\theta h = \partial_\theta \omega = \partial_\theta p_1 = \partial_\theta p_2 = 0$, at $\theta = 0$ and $\theta = \pi/2$. The input parameters are the parameters describing the halo, namely a_0 and $\mathcal{M} = M_{\text{halo}}$, and r_h , Ω_h .

To solve the system of partial differential equations, we use the same code as Ref. [127], which is publicly available at [174]. This code is a high-precision version of the code presented in Ref. [175], originally developed by one of the authors, combining a pseudospectral method with the Newton-Raphson root-finding algorithm. Details on code, its validation and accuracy are provided in the appendix of Ref. [127]. We observed exponential convergence of the code as we increased its resolution, and only accepted a solution when the absolute estimated error was below $\mathcal{O}(10^{-8})$.

III. GEODESIC MOTION

A. Equations of motion and conserved quantities

We operate on a generic metric, i.e. a stationary and axisymmetric spacetime written as

$$ds^2 = g_{tt} dt^2 + 2g_{t\varphi} dt d\varphi + g_{rr} dr^2 + g_{\theta\theta} d\theta^2 + g_{\varphi\varphi} d\varphi^2, \quad (13)$$

where the metric tensor components in (13) are functions of r and θ , and the coordinate system (t, r, θ, φ) can be chosen to be of Boyer-Lindquist [176] or quasi-isotropic type [177]. A zeroth order assumption for the evolution of an EMRI is to assume that the motion of the secondary is that of a test-particle orbiting the spacetime geometry of the primary compact object. Under this simplistic assumption, which serves, though, as a good proxy of an EMRI, for a short period of time that corresponds to some dozens of revolutions around the primary, can be described by the geodesic equations

$$\ddot{x}^\kappa + \Gamma_{\lambda\nu}^\kappa \dot{x}^\lambda \dot{x}^\nu = 0, \quad (14)$$

where $\Gamma_{\lambda\nu}^\kappa$ are the Christoffel symbols of the primary spacetime, x^κ is the four-position of the secondary, and the overdots denote differentiation with respect to proper time τ . The system of second-order, coupled differential equations resulting from Eq. (14) can be considerably

simplified using constants of motion. The spacetime metric (13) bears two Killing vector fields resulting from stationarity and axisymmetry, giving rise to two constant of motion throughout geodesic motion, i.e. the specific energy E and azimuthal angular momentum L_z of the test particle

$$E/\mu = g_{tt}\dot{t} + g_{t\varphi}\dot{\varphi}, \quad L_z/\mu = g_{t\varphi}\dot{t} + g_{\varphi\varphi}\dot{\varphi}, \quad (15)$$

where μ is the mass of the secondary particle. Equations (15) can be written as two, first-order, decoupled differential equations for the t and φ momenta, so that

$$\dot{t} = \frac{Eg_{\varphi\varphi} + L_zg_{t\varphi}}{\mu(g_{t\varphi}^2 - g_{tt}g_{\varphi\varphi})}, \quad \dot{\varphi} = \frac{Eg_{t\varphi} + L_zg_{tt}}{\mu(g_{tt}g_{\varphi\varphi} - g_{t\varphi}^2)}. \quad (16)$$

There are two remaining geodesics for r and θ which, in general, are still second-order coupled differential equations. Nevertheless, test particles in geodesic motion provide a third constant of motion, i.e., the conservation of their rest mass, or equivalently their four-velocity $g_{\lambda\nu}\dot{x}^\lambda\dot{x}^\nu = -1$. This leads to a constraint equation

$$\dot{r}^2 + \frac{g_{\theta\theta}}{g_{rr}}\dot{\theta}^2 + V_{\text{eff}} = 0, \quad (17)$$

with V_{eff} a potential of the form

$$V_{\text{eff}} \equiv \frac{1}{g_{rr}} \left(1 + \frac{g_{\varphi\varphi}E^2 + g_{tt}L_z^2 + 2g_{t\varphi}EL_z}{\mu^2(g_{tt}g_{\varphi\varphi} - g_{t\varphi}^2)} \right). \quad (18)$$

Equation (17) characterizes bound geodesic motion, through the potential V_{eff} . In turn, when $V_{\text{eff}} = 0$ a curve appears (under a choice of $\theta \in [0, \pi]$); the curve of zero velocity (CZV), where the r and θ momenta are bound to be null there, i.e., $\dot{r} = \dot{\theta} = 0$.

Under the hypothesis of another constant of motion, the geodesics can be separated into decoupled, first-order, differential equations. If though the primary spacetime does not allow for further symmetries then the r and θ motion remains coupled, and of second differential order. A Kerr BH, though, possesses a rank-two Killing tensor field, that associates the remaining components of the angular momentum with the Carter constant [128]. This successfully decouples the motion of $r(\tau)$ and $\theta(\tau)$, with τ the proper time. Since the primary configurations we will use here do not necessarily have a Carter constant (or any constant related to a higher-rank Killing tensor field), we will work under the assumption of the absence of a fourth constant of motion, and the phase space of orbits will inform us if a separation constant exists in our numerical spacetime primary. To evolve orbits we will utilize the coupled second-order differential equation system for r and θ , together with Eqs. (16) and (17), without any further symmetry assumptions.

B. Evolving geodesics on numerical backgrounds

Adopting quasi-isotropic coordinates, the line element (13) can be described through four independent

functions (f, g, h, ω) of (r, θ) , where the metric tensor components result directly from Eq. (9), i.e.,

$$g_{tt}(r, \theta) = -\frac{(1 - r_h/r)^2 f(r, \theta)}{(1 + r_h/r)^2} + \frac{(1 + r_h/r)^4 g(r, \theta) \sin^2 \theta \omega^2(r, \theta)}{r^2 f(r, \theta)}, \quad (19a)$$

$$g_{rr}(r, \theta) = \frac{(1 + r_h/r)^4 g(r, \theta) h(r, \theta)}{f(r, \theta)}, \quad (19b)$$

$$g_{\theta\theta}(r, \theta) = r^2 g_{rr}(r, \theta), \quad (19c)$$

$$g_{\varphi\varphi}(r, \theta) = \frac{r^2 (1 + r_h/r)^4 g(r, \theta) \sin^2 \theta}{f(r, \theta)}, \quad (19d)$$

$$g_{t\varphi}(r, \theta) = -\frac{(1 + r_h/r)^4 g(r, \theta) \sin^2 \theta \omega(r, \theta)}{f(r, \theta)}. \quad (19e)$$

The solutions have been found numerically following the procedure described in the previous section. The details of the numerical implementation are provided also in [127, 175]. The geodesic evolution of orbits around rotating BHs in a halo of Hernquist-type matter, uses the numerically-constructed metric tensor components (19), as in [145], and geodesics are evolved with the use of high-order interpolation functions that are constructed from the data of the metric tensor. For all simulations performed herein, we find that the constraint equation (17) is satisfied to within one part in 10^8 for the first ~ 10 thousand revolutions (and intersections through the equatorial plane). In all cases we fix the mass ratio of the EMRI to $\mu/M_{\text{BH}} = 10^{-6}$ (even though at the geodesic level it just leads to a change of scales) and choose the constant energy and azimuthal angular momentum as $E/\mu = 0.9$ and $L_z/\mu = 3M_{\text{BH}}$, respectively.

C. Non-integrability and signatures of chaos

The geodesics of Kerr BHs possess four constants of motion, namely the energy, the azimuthal angular momentum, the Carter constant and the four-velocity of the test particle. Thus, the system of equations is Liouville-integrable and does not present chaotic features [129]. Since the Carter symmetry is very fragile it may not exist when the multipolar structure of spacetime has been significantly deformed (see however Ref. [178]). The absence of a Carter symmetry, or in general any other (higher-rank) Killing tensor of spacetime, leads to the non-integrability of geodesics, since the radial and polar sectors of the geodesics are not separable, but rather form a second-order, coupled dynamical system. Some cases, where the Carter constant ceases to exist, are discussed in the Introduction. The absence of a fourth constant of motion inevitably leads to non-integrability,

which allows for chaotic effects [129]. Full-blown chaos is extremely rare, if not completely absent, at least in astrophysical EMRIs. The underlying effects of non-integrability, though, can manifest themselves indirectly in the phase space of orbits and in particular close to orbital resonances. Transient orbital resonances already affect EMRI evolution, even in Kerr where they are integrable [132, 133, 179, 180], and introduce significant dephasing effects. Non-integrable EMRIs are very likely to amplify these dephasing effects and can introduce even stronger, clear-cut phenomenology of indirect chaos [135–137].

Generic geodesics can be described by three fundamental frequencies; the frequency of oscillation from the periastron to the apastron and back, ω_r , the oscillation frequency through the equatorial plane, ω_θ and the revolution frequency ω_φ . The above orbits form irrational ratios of fundamental frequencies, thus filling densely the available phase space region they occupy. The striking majority of geodesics are generic, i.e. off-equatorial and eccentric, but in special cases where two fundamental frequencies, say ω_r/ω_θ , form a rational ratio the trajectory becomes periodic, or resonant. These special orbits are not filling their available phase space region densely, but rather after an amount of radial and polar oscillations, dictated by the rational ratio, they return to their initial position. Therefore, the transition from space-filling to non-space-filling trajectories, and back, changes the geodesic dynamics. EMRIs evolve adiabatically thus experience multiple resonance-crossings [180] that can last for a significant number of cycles, even in integrable systems. Thus, non-integrability leads to substantially enhanced resonant effects, such as cumulative dephasing and putative GW inference.

When non-integrable perturbations are present in the system, two theorems, namely the Kolmogorov-Arnold-Moser (KAM) [181, 182] and Poincaré-Birkhoff [183] theorems, dictate the modified dynamics of the orbits. The KAM theorem ensures that orbits sufficiently away from resonances, are smoothly modified but in general behave as if they were integrable. The trajectories in phase space occupy a torus defined by the constants of motion. Successive intersections of geodesics on a perpendicular 2-dimensional surface (the Poincaré surface of section) form closed curves that organize around a common central point. Those *KAM curves* form a Poincaré map, whose central point corresponds to a spherical geodesic. Close to resonances, the KAM curves disintegrate into two sets of periodic points, in accord with the Poincaré-Birkhoff theorem. The stable periodic points, from which stable resonant orbits emanate, are encapsulated inside a nest of islands, i.e., *resonant islands*, while the unstable periodic points generate chaotic orbits that surround the edges of resonant islands with thin chaotic layers. The structure around resonances of non-integrable systems is called a Birkhoff chain.

The crucial aspect of resonant islands, and their ultimate significance in EMRI dynamics, is the fact that the

rational ratio of the central, stable periodic point ω_r/ω_θ is shared throughout all geodesics residing inside the island. In a sense, integrable EMRIs experience resonances that occupy a “zero-volume point” in phase space, while non-integrable EMRIs exhibit prolonged “non-zero-volume” resonances where the secondary is locked in perfect resonance for a significant amount of revolutions around the primary. For example, in non-Kerr EMRIs, these prolonged resonances may last up to $\sim 200 - 300$ cycles depending on the primary [137, 138], without taking into account pre- and post-resonant effects [131–133] or the conservative part of gravitational self-force [184].

The existence of resonant islands is direct proof of non-integrability, therefore sketching a Poincaré map can inform us regarding the system’s symmetries. Through the Poincaré map, the rotation number can be calculated in order to search for resonant islands. It practically tracks the angle ϑ between successive intersections on KAM curves, relative to the fixed central point of the Poincaré map. The rotation number is defined as the sum of all angles ϑ measured between successive intersections of each geodesic in the surface of section, i.e.,

$$\nu_\vartheta = \frac{1}{2\pi\mathcal{N}} \sum_{i=1}^{\mathcal{N}} \vartheta_i, \quad (20)$$

where \mathcal{N} is the number of angles measured from the map. When $\mathcal{N} \rightarrow \infty$, Eq. (20) asymptotes to the ratio $\nu_\vartheta = \omega_r/\omega_\theta$ thus the rotation number can serve as a resonance browser. Consecutive rotation numbers found from different initial conditions of geodesics, by smoothly varying one of the system’s parameters while keeping the rest fixed, forms a rotation curve.

Non-integrable systems display discontinuities in the monotonicity of a rotation curve through the formation of plateaus with non-zero widths when geodesics transverse resonant islands. Therefore, the width of the plateau corresponds to the width of the resonant island and is a general measure of the timescales involved in resonant islands of non-integrable EMRIs. Inflection points can also appear in the rotation curve when trajectories pass through unstable periodic points. In what follows, we will examine the characteristic features of rotating BHs in halos of matter with geodesic evolutions, in order to search for signatures of non-integrability driven by astrophysical environments. We note that Poincaré maps and rotation curves are not the only diagnostics of chaotic phenomena. For more diagnostics that can be applied in curved spacetimes see [185].

IV. CHAOS IN RELATIVISTIC, ROTATING, NON-VACUUM BLACK HOLES

In what follows, we will use relativistic, rotating BHs in a Hernquist-type halo, with a variety of rotation parameters and matter halo compactness, while fixing the central BH mass to unity, since all our numerical evolutions lie at the geodesic level, where all observables can

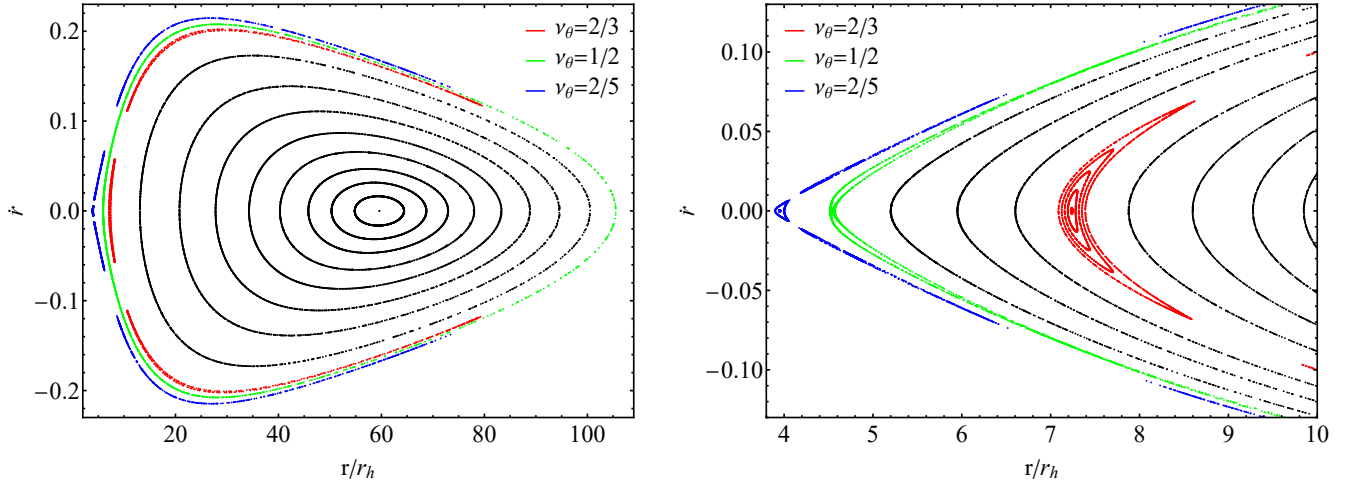


Figure 1. *Left:* Equatorial Poincaré map of generic geodesics with fixed $E/\mu = 0.9$ and $L_z/\mu = 3M_{\text{BH}}$ and varying initial position $r(0)/r_h$, where $r = r_h$ is the radius of the event horizon in quasi-isotropic coordinates. The rotating BH embedded in the Hernquist-type environment, where the geodesics are evolved, has spin $J/M_{\text{BH}}^2 \simeq 0.996$, halo compactness $M_{\text{halo}}/a_0 \simeq 10^{-1}$, and halo mass $M_{\text{halo}} \simeq 10M_{\text{BH}}$. The black curves formed around the central fixed point of the map are KAM curves that arise from orbits with irrational ratios ω_r/ω_θ , while the colored curves designate a variety of resonant islands, with rational frequency ratios. *Right:* Same as left, zoomed-in region at the strong-field regime. The red and blue islands depicted surround the stable periodic points of the resonance $\omega_r/\omega_\theta = 2/3$ and $2/5$, respectively, while the green curve corresponds to that chaotic layer that formed around the $1/2$ -resonant island due to the crossing of the unstable periodic point of the $\omega_r/\omega_\theta = 1/2$ Birkhoff chain.

be appropriately rescaled for any BH mass to simulate an EMRI, thus $M_{\text{BH}} = 1$ is merely chosen for simplicity. In turn, the test particle that will be used will have the fixed constants of motion $E/\mu = 0.9$, $L_z/\mu = 3M_{\text{BH}}$, while its mass will be chosen so that the mass-ratio is kept to $\mu/M_{\text{BH}} = 10^{-6}$, even though this is merely a scale factor in the geodesic evolution scheme. We utilize the configurations in quasi-isotropic coordinates as described in Eq. (13) and normalize the radial quasi-isotropic coordinate r with respect to the event horizon radius r_h of each configuration.

As a proof-of-principle, we numerically construct a rapidly-rotating BH with spin $J/M_{\text{BH}}^2 \simeq 0.996$ and a Hernquist-type halo with compactness $M_{\text{halo}}/a_0 \simeq 10^{-1}$, $M_{\text{halo}} \simeq 10M_{\text{BH}}$. The choice of parameters is slightly exaggerated in order to sketch a clear-cut phase-space structure of various bound geodesics, that we evolved, which might show chaotic phenomenology, as discussed in Subsection III C. The initial position of geodesics is chosen such that $r(0)$ is varying inside the CZV, while the rest of the position vector components are fixed to $\dot{r}(0) = 0$, $\theta(0) = \pi/2$ and $\dot{\theta}(0)$ is chosen in accord with the constraint equation (17) so that the resulting orbits remain bounded inside the CZV.

As each geodesic evolves, we dynamically capture the position and velocity $(r(t), \dot{r}(t))$ of the orbit, each time it crossed the equatorial plane, with $\dot{r}(t) > 0$. This process defines a KAM curve of successive intersections for each geodesic. Putting together the various KAM curves that correspond to different geodesics we sketch a Poincaré

map. In Fig. 1 we demonstrate the Poincaré map for the aforementioned matter-enriched rotating BH. It is instantly obvious that we have managed to capture, at least, three resonant island of stability shown with red, green and blue. Figure 1, left panel, shows the whole structure of orbital phase-space. The black KAM curves encircle the central point, that corresponds to a spherical orbit. This is the typical part of an integrable system. In fact, most non-integrable systems possess similar black curves that appear due to the strength of the perturbation inserted in the Hamiltonian. Therefore, the structure of phase space does not break down. Into the strong-field regime, though, numerous islands appear that do not encircle the central point of the Poincaré map, but rather encapsulated the stable periodic points of the resonance. The island structure around the resonance $2/5$ and $2/3$, shown with blue and red colors, respectively, is, according to the Poincaré-Birkhoff theorem, imprints of chaos and non-integrability of the system under consideration. Figure 1, right panel, shows a clearer zoomed-in depiction of the island nested structure. Interestingly, we do not only observe resonant islands, that surround stable periodic points, but we also find a chaotic layer, that surrounds the $1/2$ -resonant islands, not shown here. This occurs due to the fact that our meticulous scan managed to hit exactly a periodic unstable point of the $1/2$ Birkhoff chain, from which chaotic orbits emanate (shown in green). We can understand that the green structure is indeed a layer of purely chaotic orbits due to the intersections arrangement in the map, which are

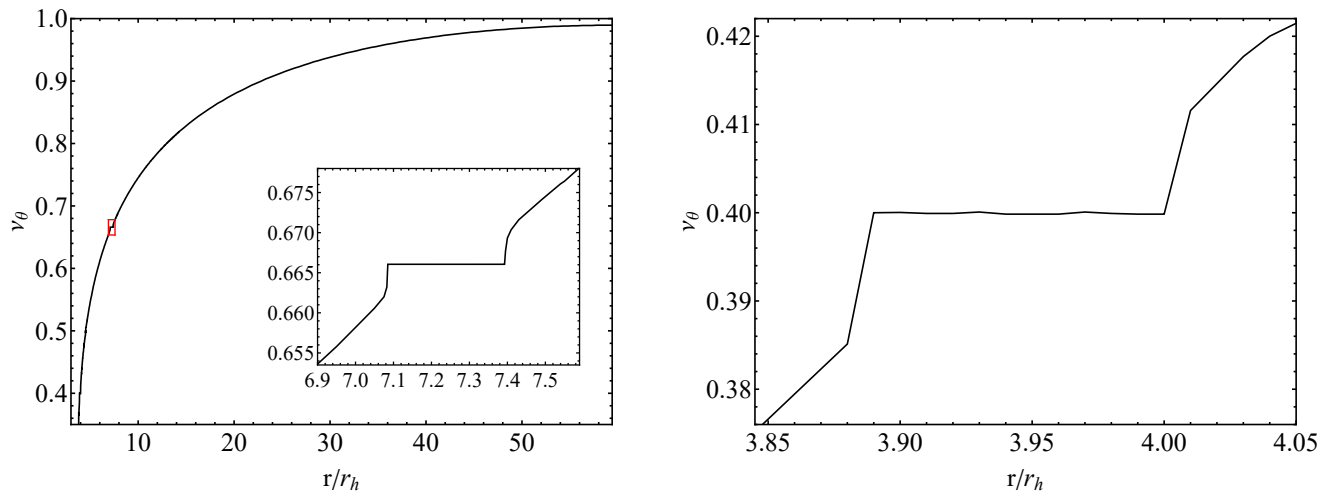


Figure 2. *Left*: Rotation curve of geodesics with fixed $E/\mu = 0.9$, $L_z/\mu = 3M_{\text{BH}}$ and varying initial position $r(0)/r_h$, resulting from an equatorial surface of section of successive geodesics. The rotating BH embedded in the Hernquist-type environment, where the geodesics are evolved, has spin $J/M_{\text{BH}}^2 \simeq 0.996$, halo compactness $M_{\text{halo}}/a_0 \simeq 10^{-1}$, and halo mass $M_{\text{halo}} \simeq 10M_{\text{BH}}$. The red box corresponds to the zoomed-in region of a resonant island, where a plateau is formed at $\nu_\vartheta = 2/3$. *Right*: Same as left configuration in the phase space vicinity of the $2/5$ -resonant island. A plateau is formed exactly at $\nu_\vartheta = 2/5$.

erratic and scattered, in contrast to KAM curves and resonant islands that present well-arranged clockwise intersections. This discussion is very relevant when one sketches the corresponding rotation curve that results from the structure of successive intersections in the map.

In Fig. 2, left panel, we demonstrate the rotation curve resulting from successive bound geodesics in the BH configuration of our study. Here, we used a much dense arrangement of successive orbits to achieve a smooth curve. For most of the rotation numbers in the curve, the curve seems to increase monotonously as $r(0)$ is increased. A more thorough look in the curve reveals the outcome of the emergence of resonant islands in the Poincaré surface. When ν_ϑ encounters the resonance $2/3$, we can clearly identify a plateau formation (see red box in Fig. 2, that corresponds to the inset in the left panel) that breaks the curve's monotonicity and effectively renders the system in study non-integrable. The inset in the left panel of Fig. 2 shows the corresponding plateau encountered when $\nu_\vartheta = 2/3 = \omega_r/\omega_\theta$, while the right panel shows the plateau formed due to the $\nu_\vartheta = 2/5$ resonant island. We note that we do not show how the crossing through the unstable periodic point $1/2$ is imprinted in the rotation curve. This is due the chaoticity of successive intersections in the Poincaré map, that leads rotation numbers that are not well-defined. The result is an erratic oscillation (or inflection point) in the rotation curve (see e.g. Fig. 9, bottom left panel, in [145]). The appearance of plateaus, and inflection points, instantly corroborates the Poincaré-Birkhoff theorem, which states that geodesics residing inside resonant islands share the same rational ratio ω_r/ω_θ , or ν_ϑ when the number of intersections measured tend to an extremely large number. In this analy-

sis, we have recorded approximately 5 to 10 thousand intersections per geodesic, that corresponds to an accuracy of 3 to 4 digits in the resulting rotation numbers. A thorough check of geodesics in further non-vacuum, rotating BH configurations, with smaller BH spin, or smaller compactness, reveals a qualitatively similar structure in the Poincaré map and the rotation curve. Hence, adding rotation to the static solution from [117], breaks integrability and leads to chaotic phenomenology, which should significantly extends the lifetime of an EMRI in resonance [135–137].

From Fig. 1 and 2, we can conclude that the resonance $2/3$ is the strongest, i.e., having the most prominent effect in EMRIs, a larger island width (and a corresponding plateau) in non-Kerr EMRIs. This is due to the multiplicity and location of the resonance $2/3$ in the strong-field regime [129]. This is the underlying reason why the literature is usually studying the effects of the $2/3$ resonance in Kerr [130–133] and non-Kerr EMRIs [135–138]. Therefore, in what follows, we present results regarding the behavior of the $2/3$ -resonant island, and in particular its width, when the spacetime parameters of the BH spin and the halo compactness are varied. The following is an order-of-magnitude analysis and will help us qualitatively understand the role of the BH spin and the halo, which combined break the Carter constant and the eventual integrability of geodesics around these objects.

A. $2/3$ island-width dependence on the spin and halo properties

Besides providing a proof-of-principle for the non-integrability of general-relativistic BHs surrounded by a

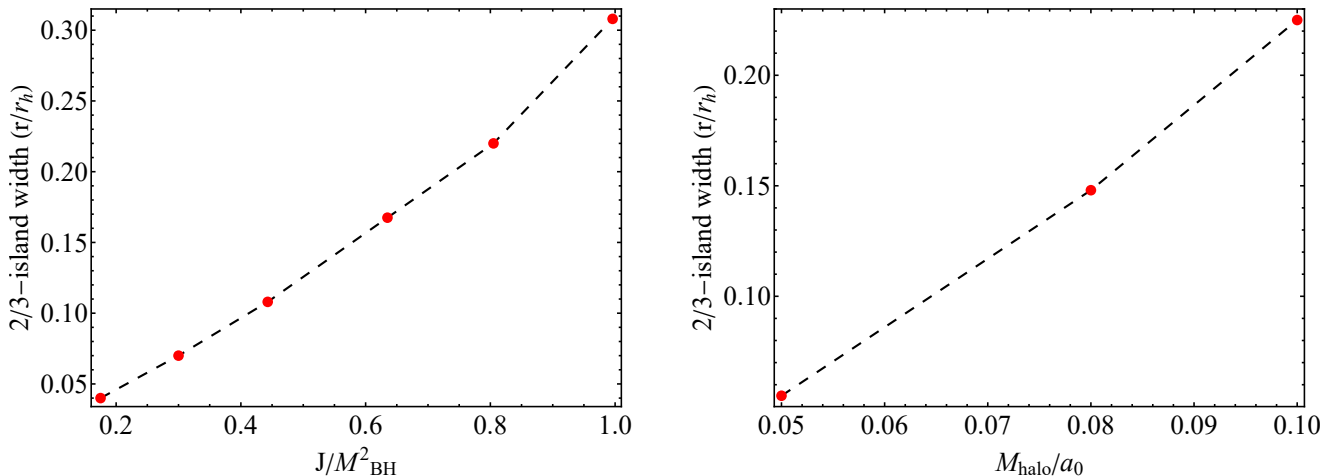


Figure 3. *Left:* Width of the 2/3-resonant islands formed in the phase space of BHs in matter halos with varying spin parameter J/M_{BH}^2 and fixed compactness $M_{\text{halo}}/a_0 \simeq 10^{-1}$, with $M_{\text{halo}} \simeq 10M_{\text{BH}}$. The island widths result from geodesic evolutions around the aforementioned configurations, with $E/\mu = 0.9$ and $L_z/\mu = 3M_{\text{BH}}$. The island width has been normalized with respect to the event horizon radius $r = r_h$ of each configuration in quasi-isotropic coordinates. *Right:* Same as left, but with fixed BH spin $J/M_{\text{BH}}^2 \simeq 0.8$ and varying compactness M_{halo}/a_0 , with $M_{\text{halo}} \simeq 10M_{\text{BH}}$. For both panels, the red dots correspond to the nine different BH configurations analyzed, while the dashed black lines correspond to crude interpolations of these values.

matter halo, it is interesting to examine how the different parameters of spacetime affect the chaotic signatures, that is the width of the resonant islands. For simplicity, we focus on the 2/3-resonant island since they provide the widest islands in phase space and corresponding plateaus in the rotation curves. Nevertheless, we have checked that the effect observed for the 2/3 resonance holds for all possible resonant island that we could probe.

Figure 3 shows how the 2/3-island width changes when we vary the BH spin and the halo compactness. In both cases, increment of the respective configuration parameter leads to an increase of the island's width. Therefore, rapidly rotating BHs surrounded by compact matter halos are expected to provide more pronounced imprints of non-integrability and chaos. Thus, although EMRIs of supermassive BHs in galaxies, surrounded by a dark matter halo may not provide clear chaotic signatures, stellar-mass BHs surrounded by a compact environment, such as BH hair or boson clouds, can produce much more apparent imprints of chaotic phenomenology. Interestingly, the latter configuration can be supported in lower mass-gap EMRIs [186].

Other studies regarding geodesics and EMRIs around non-Kerr objects [136, 187] have also demonstrated that the increment of the BH's spin leads to an increase in the resonant-island widths, therefore this result was expected and simultaneously corroborates the validity of our analysis. On the other hand, the island widths are also increasing with the halo compactness. Hence, we may extrapolate that the mass quadrupole moment, and higher multipoles are deformed in a prolate manner due to the increment of the halo's compactness (see e.g., the simi-

larities in the multipole moments of Hartle-Thorne [187] and Manko-Novikov objects [136] that produce broader islands for larger prolate deformation parameters; exactly as we observe in Fig. 3, right panel).

V. CONCLUSIONS

Resonances are choreographically well-defined periodic orbits, that return to their initial position after a number of oscillations. When a dynamical system is non-integrable, resonances are extended to resonant islands, which occupy an atypical, non-zero volume in phase space, where the periodicity of the central resonance is shared throughout the island. This leads to orbital and, most importantly, GW observables [137] that may be detected with LISA through abnormally-large cumulative dephasing events, resulting in imprecise parameter inference [130].

In order to study astrophysical EMRIs, a vacuum Kerr background is typically utilized with manual additions that express the environment's contribution to the dynamics of orbits. These approximates are not solutions to GR, but rather include the environmental effects through, either post-Newtonian schemes or with fully-relativistic treatments that mimic the dynamical interaction of the secondary with the environment. A reasonable apprehension of the main astrophysical features in GW generation and propagation has, thus, been achieved [55, 59, 60, 76]. The results so far are quite straightforward; the dynamics of EMRIs in astrophysical environments need to be treated in a fully-relativistic manner,

rather than with post-Newtonian methods, in order to capture the environmental dephasing of GWs from EMRIs [71, 74, 75]. Nevertheless, at the level of the metric, the spacetime used in contemporary studies still assumes a vacuum (integrable) Kerr BH perturbed by a non-backreacting matter environment.

Here, we surpass crude estimates, at the level of the metric, by constructing and employing general-relativistic solutions of non-vacuum GR, that describe rotating BHs at the center of matter halo environments [127]. We have evolved geodesics in order to capture the leading-order effects in EMRI dynamics. Our analysis demonstrates that when the environment backreacts on the rotating Kerr BH, it produces a non-vacuum solution of GR that significantly deforms the multipolar spacetime structure to the point that the Carter symmetry can be broken. The absence of a Carter constant alters the dynamics of geodesics around transient resonances, in a manner that designates the emergence of chaotic phenomena and non-integrability, dubbed environmental chaos. We have explicitly found resonant islands in the phase space of orbits, and thin chaotic layers that form around them, thus astrophysical environments can indeed lead to non-integrability when considered as a general-relativistic part of spacetime, and not just as a perturbation around vacuum Kerr BHs. The rotation curves corroborate the aforementioned result, due to the formation of plateaus when the geodesics are inside the respective resonant island. We, finally, performed a tentative analysis of the widths of various 2/3-resonant islands resulting by varying the BH spin and the compactness of the halo. We observe that the increment of both spin and compactness, typically, leads to larger, in span, resonant islands.

Even though our work lies only at the geodesic level, it has been shown that when radiation reaction is taken into account, even with approximate post-Newtonian fluxes of radiation, the resulting non-Kerr EMRIs can potentially spend hundreds of revolutions inside a resonant island [135, 136], where the periodicity of the central resonance is shared throughout it. The crossing of the secondary through successively-damped, “resonantly-locked”, geodesics leads to a GW observable, namely a GW glitch in the frequency evolution of the non-Kerr EMRI [137]. These glitches have a clear astrophysical interpretation [138, 144, 145], can last for weeks [138], instead of minutes or hours as in Kerr EMRIs [131], and are not associated with the typical instrumental glitches that occur due to detector noise [188–194]. Thus, we can extrapolate that if our analysis is extended at the inspiral level, then similar glitches will appear in the GW frequency evolution of general-relativistic, matter-enriched rotating EMRIs.

In the dawn of GW astronomy, the astrophysical environments around realistic, spinning BHs, such as those residing in the core of galaxies, have encountered a significant interest from the GW community, especially for sources like EMRIs that are prime targets of the LISA

mission. Our geodesic analysis demonstrates that the assumption of vacuum Kerr BHs with a perturbative, but not backreacting, addition of the astrophysical environment is not enough to describe the general-relativistic nature of the full system. By constructing a general-relativistic BH within a matter halo from first principles, using the Einstein cluster formalism [117], a complete understanding of environmental effects around BHs can be achieved at the level of the metric. Nevertheless, EMRIs evolve under radiation reaction, hence need to be treated with fully-relativistic schemes at the dynamical level as well [71, 74, 75] (instead of using Newtonian or post-Newtonian treatments).

The relativistic treatment of inspiral dynamics has already been achieved for exact GR solutions that describe matter-enriched, static and spherically-symmetric BHs [96, 123]. The final missing piece to the puzzle is to generalize the fully-relativistic treatment of EMRIs in Refs. [96, 123] to include the rotation of the primary. Nevertheless, it is easier said than done because the rotating astrophysical BHs used in this work do not have an exact form, but rather are constructed numerically. On top of that, the generalization of the relativistic techniques prescribed in [96, 123] needs to be accomplished, i.e., to transform from the Regge-Wheeler-Zerilli-matter equations (zero BH spin) to Teukolsky-matter relativistic equations (non-zero BH spin).

Even if the above generalization proves to be a thorny and time-consuming process, we can still infer some rough detectability aspects, that are an outcome of the current geodesic work. A typical resonance in a vacuum Kerr EMRI produces dephasing of dozens of radians [130, 131, 195], without taking into account the dephasing that an astrophysical environments can further introduce. Imagining that a zero-volume single point of geodesic periodicity in phase space creates such an effect in Kerr EMRIs [132], we could cautiously extrapolate that a finite volume of geodesic periodicity in phase space, which is introduced by the formation of resonant islands, will produce even bigger resonant-enhancement through unexpectedly large resonance timescales. This could be in the form of beyond-Kerr-resonance dephasing of hundreds of radians, or even abrupt dephasing kicks when the island is crossed (see Refs. [137, 138] for the resulting GW imprint of a resonance crossing). These effects alone might serve as conclusive evidence of the existence of astrophysical environments, and in general non-integrability.

Thus, it is important that resonances, and in particular possible crossings through resonant islands, to be taken into consideration with novel state-of-the-art methods (see e.g. Ref. [196]). Since GW modeling of generic Kerr EMRIs is a highly active subject of research, so does the GW modeling of resonant-island crossings should be explored for non-vacuum, general-relativistic spinning EMRIs. The combination of environmental effects, resonances, and astrophysical chaos, could form, in the future, the amalgamation of a well-explored branch

of precise GW modeling for realistic EMRIs within astrophysical environments. One, though, needs to stay cautious for potential modifications of gravity, or supermassive exotic compact object primaries, in order to avoid degeneracies between environmental and non-GR chaotic effects in EMRIs.

ACKNOWLEDGMENTS

The authors would like to warmly thank Vitor Cardoso for fruitful discussions. K.D. acknowledges financial support provided by FCT-Fundação para a Ciência e a Tecnologia, I.P., under the Scientific Employment Stimulus – Individual Call – Grant No. 2023.07417.CEECIND/CP2830/CT0008. P.F. is funded by the Deutsche Forschungsgemeinschaft (DFG, German Research Foundation) under Germany’s Excellence Strategy EXC 2181/1 - 390900948 (the Heidelberg STRUCTURES Excellence Cluster). This project has received funding from the European Union’s Horizon MSCA-2022 research and innovation programme “Einstein Waves” under grant agreement No. 101131233.

-
- [1] R. Abbott *et al.* (KAGRA, VIRGO, LIGO Scientific), GWTC-3: Compact Binary Coalescences Observed by LIGO and Virgo during the Second Part of the Third Observing Run, *Phys. Rev. X* **13**, 041039 (2023), [arXiv:2111.03606 \[gr-qc\]](#).
 - [2] D. Davis *et al.* (LIGO), LIGO detector characterization in the second and third observing runs, *Class. Quant. Grav.* **38**, 135014 (2021), [arXiv:2101.11673 \[astro-ph.IM\]](#).
 - [3] L. Barack *et al.*, Black holes, gravitational waves and fundamental physics: a roadmap, *Class. Quant. Grav.* **36**, 143001 (2019), [arXiv:1806.05195 \[gr-qc\]](#).
 - [4] B. P. Abbott *et al.* (LIGO Scientific, Virgo), Observation of Gravitational Waves from a Binary Black Hole Merger, *Phys. Rev. Lett.* **116**, 061102 (2016), [arXiv:1602.03837 \[gr-qc\]](#).
 - [5] P. Amaro-Seoane *et al.* (LISA), Laser Interferometer Space Antenna (2017), [arXiv:1702.00786 \[astro-ph.IM\]](#).
 - [6] B. F. Schutz, Gravitational wave astronomy, *Class. Quant. Grav.* **16**, A131 (1999), [arXiv:gr-qc/9911034](#).
 - [7] M. Bailes *et al.*, Gravitational-wave physics and astronomy in the 2020s and 2030s, *Nature Rev. Phys.* **3**, 344 (2021).
 - [8] E. Barausse *et al.*, Prospects for Fundamental Physics with LISA, *Gen. Rel. Grav.* **52**, 81 (2020), [arXiv:2001.09793 \[gr-qc\]](#).
 - [9] K. G. Arun *et al.* (LISA), New horizons for fundamental physics with LISA, *Living Rev. Rel.* **25**, 4 (2022), [arXiv:2205.01597 \[gr-qc\]](#).
 - [10] N. Karnesis *et al.*, The Laser Interferometer Space Antenna mission in Greece White Paper (2022), [arXiv:2209.04358 \[gr-qc\]](#).
 - [11] P. Amaro-Seoane *et al.*, Astrophysics with the Laser Interferometer Space Antenna (2022), [arXiv:2203.06016 \[gr-qc\]](#).
 - [12] P. A. Seoane *et al.* (LISA), Astrophysics with the Laser Interferometer Space Antenna, *Living Rev. Rel.* **26**, 2 (2023), [arXiv:2203.06016 \[gr-qc\]](#).
 - [13] A. M. Ghez, B. L. Klein, M. Morris, and E. E. Becklin, High proper motion stars in the vicinity of Sgr A*: Evidence for a supermassive black hole at the center of our galaxy, *Astrophys. J.* **509**, 678 (1998), [arXiv:astro-ph/9807210](#).
 - [14] R. Genzel, F. Eisenhauer, and S. Gillessen, The Galactic Center massive black hole and nuclear star cluster, *Reviews of Modern Physics* **82**, 3121 (2010), [arXiv:1006.0064 \[astro-ph.GA\]](#).
 - [15] P. Amaro-Seoane, J. R. Gair, M. Freitag, M. Coleman Miller, I. Mandel, C. J. Cutler, and S. Babak, Astrophysics, detection and science applications of intermediate- and extreme mass-ratio inspirals, *Class. Quant. Grav.* **24**, R113 (2007), [arXiv:astro-ph/0703495](#).
 - [16] J. R. Gair, S. Babak, A. Sesana, P. Amaro-Seoane, E. Barausse, C. P. L. Berry, E. Berti, and C. Sopuerta, Prospects for observing extreme-mass-ratio inspirals with LISA, *J. Phys. Conf. Ser.* **840**, 012021 (2017), [arXiv:1704.00009 \[astro-ph.GA\]](#).
 - [17] S. Babak, J. Gair, A. Sesana, E. Barausse, C. F. Sopuerta, C. P. L. Berry, E. Berti, P. Amaro-Seoane, A. Petiteau, and A. Klein, Science with the space-based interferometer LISA. V: Extreme mass-ratio inspirals, *Phys. Rev. D* **95**, 103012 (2017), [arXiv:1703.09722 \[gr-qc\]](#).
 - [18] P. Auclair *et al.* (LISA Cosmology Working Group), Cosmology with the Laser Interferometer Space Antenna, *Living Rev. Rel.* **26**, 5 (2023), [arXiv:2204.05434 \[astro-ph.CO\]](#).
 - [19] Y. Raveh and H. B. Perets, Extreme mass-ratio gravitational-wave sources: Mass segregation and post binary tidal-disruption captures, *Mon. Not. Roy. Astron. Soc.* **501**, 5012 (2021), [arXiv:2011.13952 \[astro-ph.GA\]](#).
 - [20] P. Amaro-Seoane, Relativistic dynamics and extreme mass ratio inspirals, *Living Rev. Rel.* **21**, 4 (2018), [arXiv:1205.5240 \[astro-ph.CO\]](#).
 - [21] Z. Pan and H. Yang, Formation Rate of Extreme Mass Ratio Inspirals in Active Galactic Nuclei, *Phys. Rev. D* **103**, 103018 (2021), [arXiv:2101.09146 \[astro-ph.HE\]](#).
 - [22] Z. Pan, Z. Lyu, and H. Yang, Wet extreme mass ratio inspirals may be more common for spaceborne gravitational wave detection, *Phys. Rev. D* **104**, 063007 (2021), [arXiv:2104.01208 \[astro-ph.HE\]](#).
 - [23] A. J. K. Chua, M. L. Katz, N. Warburton, and S. A. Hughes, Rapid generation of fully relativistic extreme-mass-ratio-inspiral waveform templates for LISA data analysis, *Phys. Rev. Lett.* **126**, 051102 (2021), [arXiv:2008.06071 \[gr-qc\]](#).

- [24] M. L. Katz, A. J. K. Chua, L. Speri, N. Warburton, and S. A. Hughes, Fast extreme-mass-ratio-inspiral waveforms: New tools for millihertz gravitational-wave data analysis, *Phys. Rev. D* **104**, 064047 (2021), [arXiv:2104.04582 \[gr-qc\]](#).
- [25] N. Afshordi *et al.* (LISA Consortium Waveform Working Group), Waveform Modelling for the Laser Interferometer Space Antenna (2023), [arXiv:2311.01300 \[gr-qc\]](#).
- [26] K. Glampedakis and S. Babak, Mapping spacetimes with LISA: Inspirals of a test-body in a ‘quasi-Kerr’ field, *Class. Quant. Grav.* **23**, 4167 (2006), [arXiv:gr-qc/0510057](#).
- [27] J. R. Gair, M. Vallisneri, S. L. Larson, and J. G. Baker, Testing General Relativity with Low-Frequency, Space-Based Gravitational-Wave Detectors, *Living Rev. Rel.* **16**, 7 (2013), [arXiv:1212.5575 \[gr-qc\]](#).
- [28] N. Yunes, P. Pani, and V. Cardoso, Gravitational Waves from Quasicircular Extreme Mass-Ratio Inspirals as Probes of Scalar-Tensor Theories, *Phys. Rev. D* **85**, 102003 (2012), [arXiv:1112.3351 \[gr-qc\]](#).
- [29] V. Cardoso and L. Gualtieri, Testing the black hole ‘no-hair’ hypothesis, *Class. Quant. Grav.* **33**, 174001 (2016), [arXiv:1607.03133 \[gr-qc\]](#).
- [30] P. Pani, V. Cardoso, and L. Gualtieri, Gravitational waves from extreme mass-ratio inspirals in Dynamical Chern-Simons gravity, *Phys. Rev. D* **83**, 104048 (2011), [arXiv:1104.1183 \[gr-qc\]](#).
- [31] V. Cardoso, S. Chakrabarti, P. Pani, E. Berti, and L. Gualtieri, Floating and sinking: The Imprint of massive scalars around rotating black holes, *Phys. Rev. Lett.* **107**, 241101 (2011), [arXiv:1109.6021 \[gr-qc\]](#).
- [32] P. Canizares, J. R. Gair, and C. F. Sopuerta, Testing Chern-Simons Modified Gravity with Gravitational-Wave Detections of Extreme-Mass-Ratio Binaries, *Phys. Rev. D* **86**, 044010 (2012), [arXiv:1205.1253 \[gr-qc\]](#).
- [33] E. Berti *et al.*, Testing General Relativity with Present and Future Astrophysical Observations, *Class. Quant. Grav.* **32**, 243001 (2015), [arXiv:1501.07274 \[gr-qc\]](#).
- [34] A. J. K. Chua, S. Hee, W. J. Handley, E. Higgs, C. J. Moore, J. R. Gair, M. P. Hobson, and A. N. Lasenby, Towards a framework for testing general relativity with extreme-mass-ratio-inspiral observations, *Mon. Not. Roy. Astron. Soc.* **478**, 28 (2018), [arXiv:1803.10210 \[gr-qc\]](#).
- [35] E. Berti *et al.*, Tests of General Relativity and Fundamental Physics with Space-based Gravitational Wave Detectors (2019), [arXiv:1903.02781 \[astro-ph.HE\]](#).
- [36] J. Zhang and H. Yang, Gravitational floating orbits around hairy black holes, *Phys. Rev. D* **99**, 064018 (2019), [arXiv:1808.02905 \[gr-qc\]](#).
- [37] C. P. L. Berry, S. A. Hughes, C. F. Sopuerta, A. J. K. Chua, A. Heffernan, K. Holley-Bockelmann, D. P. Mihaylov, M. C. Miller, and A. Sesana, The unique potential of extreme mass-ratio inspirals for gravitational-wave astronomy, *Bull. Am. Astron. Soc.* **51**, 42 (2019), [arXiv:1903.03686 \[astro-ph.HE\]](#).
- [38] A. Cárdenas-Avendaño and C. F. Sopuerta, Testing Gravity with Extreme-Mass-Ratio Inspirals (2024) [arXiv:2401.08085 \[gr-qc\]](#).
- [39] E. Berti, Tests of general relativity with future detectors, *Gen. Rel. Grav.* **56**, 145 (2024).
- [40] S. Datta and S. Bose, Probing the nature of central objects in extreme-mass-ratio inspirals with gravitational waves, *Phys. Rev. D* **99**, 084001 (2019), [arXiv:1902.01723 \[gr-qc\]](#).
- [41] O. A. Hannuksela, K. W. K. Wong, R. Brito, E. Berti, and T. G. F. Li, Probing the existence of ultralight bosons with a single gravitational-wave measurement, *Nature Astron.* **3**, 447 (2019), [arXiv:1804.09659 \[astro-ph.HE\]](#).
- [42] A. Maselli, N. Franchini, L. Gualtieri, and T. P. Sotiriou, Detecting scalar fields with Extreme Mass Ratio Inspirals, *Phys. Rev. Lett.* **125**, 141101 (2020), [arXiv:2004.11895 \[gr-qc\]](#).
- [43] A. Maselli, N. Franchini, L. Gualtieri, T. P. Sotiriou, S. Barsanti, and P. Pani, Detecting fundamental fields with LISA observations of gravitational waves from extreme mass-ratio inspirals, *Nature Astron.* **6**, 464 (2022), [arXiv:2106.11325 \[gr-qc\]](#).
- [44] S. Barsanti, A. Maselli, T. P. Sotiriou, and L. Gualtieri, Detecting massive scalar fields with Extreme Mass-Ratio Inspirals (2022), [arXiv:2212.03888 \[gr-qc\]](#).
- [45] S. Barsanti, N. Franchini, L. Gualtieri, A. Maselli, and T. P. Sotiriou, Extreme mass-ratio inspirals as probes of scalar fields: Eccentric equatorial orbits around Kerr black holes, *Phys. Rev. D* **106**, 044029 (2022), [arXiv:2203.05003 \[gr-qc\]](#).
- [46] S. Mitra, S. Chakraborty, R. Vicente, and J. C. Feng, Probing the quantum nature of black holes with ultralight boson environments, *Phys. Rev. D* **110**, 084012 (2024), [arXiv:2312.06783 \[gr-qc\]](#).
- [47] C. Zhang and Y. Gong, Probing new fundamental fields with extreme mass ratio inspirals, *Phys. Rev. D* **110**, 104052 (2024), [arXiv:2407.07449 \[gr-qc\]](#).
- [48] J. Lestingi, E. Cannizzaro, and P. Pani, Extreme mass-ratio inspirals as probes of fundamental dipoles, *Phys. Rev. D* **109**, 044052 (2024), [arXiv:2310.07772 \[gr-qc\]](#).
- [49] M. Della Rocca, S. Barsanti, L. Gualtieri, and A. Maselli, Extreme mass-ratio inspirals as probes of scalar fields: Inclined circular orbits around Kerr black holes, *Phys. Rev. D* **109**, 104079 (2024), [arXiv:2401.09542 \[gr-qc\]](#).
- [50] P. Gondolo and J. Silk, Dark matter annihilation at the galactic center, *Phys. Rev. Lett.* **83**, 1719 (1999), [arXiv:astro-ph/9906391](#).
- [51] G. Sigl, J. Schnittman, and A. Buonanno, Gravitational-wave background from compact objects embedded in AGN accretion disks, *Phys. Rev. D* **75**, 024034 (2007), [arXiv:astro-ph/0610680](#).
- [52] M. Preto and P. Amaro-Seoane, On strong mass segregation around a massive black hole: Implications for lower-frequency gravitational-wave astrophysics, *Astrophys. J. Lett.* **708**, L42 (2010), [arXiv:0910.3206 \[astro-ph.GA\]](#).
- [53] N. Yunes, B. Kocsis, A. Loeb, and Z. Haiman, Imprint of Accretion Disk-Induced Migration on Gravitational Waves from Extreme Mass Ratio Inspirals, *Phys. Rev. Lett.* **107**, 171103 (2011), [arXiv:1103.4609 \[astro-ph.CO\]](#).
- [54] B. Kocsis, N. Yunes, and A. Loeb, Observable Signatures of EMRI Black Hole Binaries Embedded in Thin Accretion Disks, *Phys. Rev. D* **84**, 024032 (2011), [arXiv:1104.2322 \[astro-ph.GA\]](#).
- [55] C. F. B. Macedo, P. Pani, V. Cardoso, and L. C. B. Crispino, Into the lair: gravitational-wave signatures of dark matter, *Astrophys. J.* **774**, 48 (2013), [arXiv:1302.2646 \[gr-qc\]](#).
- [56] L. Sadeghian, F. Ferrer, and C. M. Will, Dark mat-

- ter distributions around massive black holes: A general relativistic analysis, *Phys. Rev. D* **88**, 063522 (2013), [arXiv:1305.2619 \[astro-ph.GA\]](#).
- [57] F. Ferrer, A. M. da Rosa, and C. M. Will, Dark matter spikes in the vicinity of Kerr black holes, *Phys. Rev. D* **96**, 083014 (2017), [arXiv:1707.06302 \[astro-ph.CO\]](#).
- [58] O. A. Hannuksela, K. C. Y. Ng, and T. G. F. Li, Extreme dark matter tests with extreme mass ratio inspirals, *Phys. Rev. D* **102**, 103022 (2020), [arXiv:1906.11845 \[astro-ph.CO\]](#).
- [59] V. Cardoso and A. Maselli, Constraints on the astrophysical environment of binaries with gravitational-wave observations, *Astron. Astrophys.* **644**, A147 (2020), [arXiv:1909.05870 \[astro-ph.HE\]](#).
- [60] L. Polcar, G. Lukes-Gerakopoulos, and V. Witzany, Extreme mass ratio inspirals into black holes surrounded by matter, *Phys. Rev. D* **106**, 044069 (2022), [arXiv:2205.08516 \[gr-qc\]](#).
- [61] L. Speri, A. Antonelli, L. Sberna, S. Babak, E. Barausse, J. R. Gair, and M. L. Katz, Measuring accretion-disk effects with gravitational waves from extreme mass ratio inspirals (2022), [arXiv:2207.10086 \[gr-qc\]](#).
- [62] F. Duque, C. F. B. Macedo, R. Vicente, and V. Cardoso, Extreme-Mass-Ratio Inspirals in Ultralight Dark Matter, *Phys. Rev. Lett.* **133**, 121404 (2024), [arXiv:2312.06767 \[gr-qc\]](#).
- [63] R. Brito and S. Shah, Extreme mass-ratio inspirals into black holes surrounded by scalar clouds, *Phys. Rev. D* **108**, 084019 (2023), [Erratum: *Phys. Rev. D* **110**, 109902 (2024)], [arXiv:2307.16093 \[gr-qc\]](#).
- [64] D. Traykova, K. Clough, T. Helfer, E. Berti, P. G. Ferreira, and L. Hui, Dynamical friction from scalar dark matter in the relativistic regime, *Phys. Rev. D* **104**, 103014 (2021), [arXiv:2106.08280 \[gr-qc\]](#).
- [65] D. Traykova, R. Vicente, K. Clough, T. Helfer, E. Berti, P. G. Ferreira, and L. Hui, Relativistic drag forces on black holes from scalar dark matter clouds of all sizes, *Phys. Rev. D* **108**, L121502 (2023), [arXiv:2305.10492 \[gr-qc\]](#).
- [66] S. Chatterjee, S. Mondal, and P. Basu, Detectability of gas-rich E/IMRI's in LISA band: observable signature of transonic accretion flow, *Mon. Not. Roy. Astron. Soc.* **526**, 5612 (2023), [arXiv:2307.12144 \[astro-ph.HE\]](#).
- [67] A. Santini, D. Gerosa, R. Cotesta, and E. Berti, Black-hole mergers in disklike environments could explain the observed q - χ_{eff} correlation, *Phys. Rev. D* **108**, 083033 (2023), [arXiv:2308.12998 \[astro-ph.HE\]](#).
- [68] S. Roy and R. Vicente, Compact binary coalescences in dense gaseous environments can pose as ones in vacuum, *Phys. Rev. D* **111**, 084037 (2025), [arXiv:2410.16388 \[gr-qc\]](#).
- [69] F. Duque, S. Kejriwal, L. Sberna, L. Speri, and J. Gair, Constraining accretion physics with gravitational waves from eccentric extreme-mass-ratio inspirals, *Phys. Rev. D* **111**, 084006 (2025), [arXiv:2411.03436 \[gr-qc\]](#).
- [70] Z. Lyu, Z. Pan, J. Mao, N. Jiang, and H. Yang, Science Opportunities of Wet Extreme Mass-Ratio Inspirals (2024), [arXiv:2501.03252 \[astro-ph.HE\]](#).
- [71] C. Dyson, T. F. M. Spijksma, R. Brito, M. van de Meent, and S. Dolan, Environmental Effects in Extreme-Mass-Ratio Inspirals: Perturbations to the Environment in Kerr Spacetimes, *Phys. Rev. Lett.* **134**, 211403 (2025), [arXiv:2501.09806 \[gr-qc\]](#).
- [72] S. Mitra, N. Speeney, S. Chakraborty, and E. Berti, Extreme mass ratio inspirals in rotating dark matter spikes (2025), [arXiv:2505.04697 \[gr-qc\]](#).
- [73] D. Blas, S. Gasparotto, and R. Vicente, Searching for ultralight dark matter through frequency modulation of gravitational waves, *Phys. Rev. D* **111**, 042008 (2025), [arXiv:2410.07330 \[hep-ph\]](#).
- [74] R. Vicente, T. K. Karydas, and G. Bertone, A fully relativistic treatment of EMRIs in collisionless environments (2025), [arXiv:2505.09715 \[gr-qc\]](#).
- [75] L. Polcar and V. Witzany, Towards relativistic inspirals into black holes surrounded by matter (2025), [arXiv:2507.15720 \[gr-qc\]](#).
- [76] G. Caneva Santoro, S. Roy, R. Vicente, M. Haney, O. J. Piccinni, W. Del Pozzo, and M. Martinez, First Constraints on Compact Binary Environments from LIGO-Virgo Data, *Phys. Rev. Lett.* **132**, 251401 (2024), [arXiv:2309.05061 \[gr-qc\]](#).
- [77] L. Zwick, J. Takátsy, P. Saini, K. Hendriks, J. Samsing, C. Tiede, C. Rowan, and A. A. Trani, Environmental effects in stellar mass gravitational wave sources I: Expected fraction of signals with significant dephasing in the dynamical and AGN channels (2025), [arXiv:2503.24084 \[astro-ph.HE\]](#).
- [78] L. Zwick, K. Hendriks, D. O'Neill, J. Takátsy, P. Kirkeberg, C. Tiede, J. Stegmann, J. Samsing, and D. J. D'Orazio, Dissecting environmental effects with eccentric gravitational wave sources (2025), [arXiv:2506.09140 \[astro-ph.HE\]](#).
- [79] K. Destounis and F. Duque, Black-hole spectroscopy: quasinormal modes, ringdown stability and the pseudospectrum (2023) [arXiv:2308.16227 \[gr-qc\]](#).
- [80] J. L. Jaramillo, R. Panosso Macedo, and L. Al Sheikh, Pseudospectrum and Black Hole Quasinormal Mode Instability, *Phys. Rev. X* **11**, 031003 (2021), [arXiv:2004.06434 \[gr-qc\]](#).
- [81] J. L. Jaramillo, R. Panosso Macedo, and L. A. Sheikh, Gravitational Wave Signatures of Black Hole Quasinormal Mode Instability, *Phys. Rev. Lett.* **128**, 211102 (2022), [arXiv:2105.03451 \[gr-qc\]](#).
- [82] M. H.-Y. Cheung, K. Destounis, R. P. Macedo, E. Berti, and V. Cardoso, Destabilizing the Fundamental Mode of Black Holes: The Elephant and the Flea, *Phys. Rev. Lett.* **128**, 111103 (2022), [arXiv:2111.05415 \[gr-qc\]](#).
- [83] K. Destounis, R. P. Macedo, E. Berti, V. Cardoso, and J. L. Jaramillo, Pseudospectrum of Reissner-Nordström black holes: Quasinormal mode instability and universality, *Phys. Rev. D* **104**, 084091 (2021), [arXiv:2107.09673 \[gr-qc\]](#).
- [84] V. Boyanov, K. Destounis, R. Panosso Macedo, V. Cardoso, and J. L. Jaramillo, Pseudospectrum of horizonless compact objects: A bootstrap instability mechanism, *Phys. Rev. D* **107**, 064012 (2023), [arXiv:2209.12950 \[gr-qc\]](#).
- [85] S. Sarkar, M. Rahman, and S. Chakraborty, Perturbing the perturbed: Stability of quasinormal modes in presence of a positive cosmological constant, *Phys. Rev. D* **108**, 104002 (2023), [arXiv:2304.06829 \[gr-qc\]](#).
- [86] K. Destounis, V. Boyanov, and R. Panosso Macedo, Pseudospectrum of de Sitter black holes, *Phys. Rev. D* **109**, 044023 (2024), [arXiv:2312.11630 \[gr-qc\]](#).
- [87] V. Boyanov, V. Cardoso, K. Destounis, J. L. Jaramillo, and R. Panosso Macedo, Structural aspects of the anti-de Sitter black hole pseudospectrum, *Phys. Rev. D* **109**, 064068 (2024), [arXiv:2312.11998 \[gr-qc\]](#).

- [88] D. Areán, D. G. Fariña, and K. Landsteiner, Pseudospectra of holographic quasinormal modes, *JHEP* **12**, 187, [arXiv:2307.08751 \[hep-th\]](#).
- [89] B. Cownden, C. Pantelidou, and M. Zilhão, The pseudospectra of black holes in AdS, *JHEP* **05**, 202, [arXiv:2312.08352 \[gr-qc\]](#).
- [90] A. Courty, K. Destounis, and P. Pani, Spectral instability of quasinormal modes and strong cosmic censorship, *Phys. Rev. D* **108**, 104027 (2023), [arXiv:2307.11155 \[gr-qc\]](#).
- [91] R. F. Rosato, K. Destounis, and P. Pani, Ringdown stability: Graybody factors as stable gravitational-wave observables, *Phys. Rev. D* **110**, L121501 (2024), [arXiv:2406.01692 \[gr-qc\]](#).
- [92] V. Boyanov, On destabilising quasi-normal modes with a radially concentrated perturbation, *Front. in Phys.* **12**, 1511757 (2024), [arXiv:2410.11547 \[gr-qc\]](#).
- [93] R.-G. Cai, L.-M. Cao, J.-N. Chen, Z.-K. Guo, L.-B. Wu, and Y.-S. Zhou, Pseudospectrum for the Kerr black hole with spin $s=0$ case, *Phys. Rev. D* **111**, 084011 (2025), [arXiv:2501.02522 \[gr-qc\]](#).
- [94] T. F. M. Spieksma, V. Cardoso, G. Carullo, M. Della Rocca, and F. Duque, Black Hole Spectroscopy in Environments: Detectability Prospects, *Phys. Rev. Lett.* **134**, 081402 (2025), [arXiv:2409.05950 \[gr-qc\]](#).
- [95] S. Datta, Black holes immersed in dark matter: Energy condition and sound speed, *Phys. Rev. D* **109**, 104042 (2024), [arXiv:2312.01277 \[gr-qc\]](#).
- [96] S. Datta and A. Maselli, A multi-parameter expansion for the evolution of asymmetric binaries in astrophysical environments (2025), [arXiv:2507.04471 \[gr-qc\]](#).
- [97] F. G. Pease, The rotation and radial velocity of the spiral nebula ngcc4594, *Publications of the Astronomical Society of the Pacific* **28**, 191 (1916).
- [98] F. G. Pease, The rotation and radial velocity of the central part of the andromeda nebula, *Proceedings of the National Academy of Sciences* **4**, 21 (1918), <https://www.pnas.org/doi/pdf/10.1073/pnas.4.1.21>.
- [99] M. Schwarzschild, Mass distribution and mass-luminosity ratio in galaxies, *The Astronomical Journal* **59**, 273 (1954).
- [100] B. Lindblad, Galactic dynamics, in *Astrophysik IV: Sternsysteme / Astrophysics IV: Stellar Systems*, edited by S. Flügge (Springer Berlin Heidelberg, Berlin, Heidelberg, 1959) pp. 21–99.
- [101] G. de Vaucouleurs, Classification and Morphology of External Galaxies., *Handbuch der Physik* **53**, 275 (1959).
- [102] G. de Vaucouleurs and K. Freeman, Structure and dynamics of barred spiral galaxies, in particular of the magellanic type, *Vistas in Astronomy* **14**, 163 (1972).
- [103] G. Burbidge, On the masses and relative velocities of galaxies., *The Astrophysical Journal Letters* **196**, L7 (1975).
- [104] P. C. van der Kruit and A. Bosma, The rotation curves and orientation parameters of the spiral galaxies NGC 2715, 5033 and 5055., *Astronomy and Astrophysics* **34**, 259 (1978).
- [105] Y. Sofue and V. Rubin, Rotation curves of spiral galaxies, *Ann. Rev. Astron. Astrophys.* **39**, 137 (2001), [arXiv:astro-ph/0010594](#).
- [106] C. R. Canizares, G. W. Clark, T. H. Markert, C. Berg, M. Smedira, D. Bardas, H. Schnopper, and K. Kalata, High-resolution X-ray spectroscopy of M87 with the Einstein Observatory: the detection of an O VIII emission line., *The Astrophysical Journal Letters* **234**, L33 (1979).
- [107] C. R. Canizares, G. W. Clark, J. G. Jernigan, and T. H. Markert, X-ray spectroscopy of the galaxy M 87: radiative accretion of the hot plasma halo., *Astrophys. J.* **262**, 33 (1982).
- [108] S. P. Boughn and P. R. Saulson, Infrared photometry of the halo of M 87., *The Astrophysical Journal Letters* **265**, L55 (1983).
- [109] K. Akiyama *et al.* (Event Horizon Telescope), First M87 Event Horizon Telescope Results. I. The Shadow of the Supermassive Black Hole, *Astrophys. J. Lett.* **875**, L1 (2019), [arXiv:1906.11238 \[astro-ph.GA\]](#).
- [110] K. Akiyama *et al.* (Event Horizon Telescope), First Sagittarius A* Event Horizon Telescope Results. I. The Shadow of the Supermassive Black Hole in the Center of the Milky Way, *Astrophys. J. Lett.* **930**, L12 (2022).
- [111] S. Taylor and E. Poisson, Nonrotating black hole in a post-Newtonian tidal environment, *Phys. Rev. D* **78**, 084016 (2008), [arXiv:0806.3052 \[gr-qc\]](#).
- [112] E. Poisson and E. Corrigan, Nonrotating black hole in a post-Newtonian tidal environment II, *Phys. Rev. D* **97**, 124048 (2018), [arXiv:1804.01848 \[gr-qc\]](#).
- [113] K. Eda, Y. Itoh, S. Kuroyanagi, and J. Silk, New Probe of Dark-Matter Properties: Gravitational Waves from an Intermediate-Mass Black Hole Embedded in a Dark-Matter Minispike, *Phys. Rev. Lett.* **110**, 221101 (2013), [arXiv:1301.5971 \[gr-qc\]](#).
- [114] N. Tamanini, A. Klein, C. Bonvin, E. Barausse, and C. Caprini, Peculiar acceleration of stellar-origin black hole binaries: Measurement and biases with LISA, *Phys. Rev. D* **101**, 063002 (2020), [arXiv:1907.02018 \[astro-ph.IM\]](#).
- [115] B. J. Kavanagh, D. A. Nichols, G. Bertone, and D. Gaggero, Detecting dark matter around black holes with gravitational waves: Effects of dark-matter dynamics on the gravitational waveform, *Phys. Rev. D* **102**, 083006 (2020), [arXiv:2002.12811 \[gr-qc\]](#).
- [116] A. U. P. Ylla, Y. Koga, and C.-M. Yoo, Test particle motion around a black hole dressed with a spherically symmetric stationary fluid (2025), [arXiv:2504.21755 \[gr-qc\]](#).
- [117] V. Cardoso, K. Destounis, F. Duque, R. P. Macedo, and A. Maselli, Black holes in galaxies: Environmental impact on gravitational-wave generation and propagation, *Phys. Rev. D* **105**, L061501 (2022), [arXiv:2109.00005 \[gr-qc\]](#).
- [118] L. Hernquist, An Analytical Model for Spherical Galaxies and Bulges, *Astrophys. J.* **356**, 359 (1990).
- [119] Z. Stuchlík and J. Vrba, Supermassive black holes surrounded by dark matter modeled as anisotropic fluid: epicyclic oscillations and their fitting to observed QPOs, *JCAP* **11** (11), 059, [arXiv:2110.07411 \[gr-qc\]](#).
- [120] R. A. Konoplya and A. Zhidenko, Solutions of the Einstein Equations for a Black Hole Surrounded by a Galactic Halo, *Astrophys. J.* **933**, 166 (2022), [arXiv:2202.02205 \[gr-qc\]](#).
- [121] K. Jusufi, Black holes surrounded by Einstein clusters as models of dark matter fluid (2022), [arXiv:2202.00010 \[gr-qc\]](#).
- [122] L. Pezzella, K. Destounis, A. Maselli, and V. Cardoso, Quasinormal modes of black holes embedded in halos of matter, *Phys. Rev. D* **111**, 064026 (2025),

- arXiv:2412.18651 [gr-qc].
- [123] V. Cardoso, K. Destounis, F. Duque, R. Panosso Macedo, and A. Maselli, Gravitational waves from extreme-mass-ratio systems in astrophysical environments (2022), arXiv:2210.01133 [gr-qc].
 - [124] N. Speeney, E. Berti, V. Cardoso, and A. Maselli, Black holes surrounded by generic matter distributions: Polar perturbations and energy flux, *Phys. Rev. D* **109**, 084068 (2024), arXiv:2401.00932 [gr-qc].
 - [125] E. Figueiredo, A. Maselli, and V. Cardoso, Black holes surrounded by generic dark matter profiles: appearance and gravitational-wave emission (2023), arXiv:2303.08183 [gr-qc].
 - [126] S. Gliorio, E. Berti, A. Maselli, and N. Speeney, Extreme mass ratio inspirals in dark matter halos: dynamics and distinguishability of halo models (2025), arXiv:2503.16649 [gr-qc].
 - [127] P. G. S. Fernandes and V. Cardoso, Spinning black holes in astrophysical environments (2025), arXiv:2507.04389 [gr-qc].
 - [128] B. Carter, Global structure of the Kerr family of gravitational fields, *Phys. Rev.* **174**, 1559 (1968).
 - [129] G. Contopoulos, *Order and Chaos in Dynamical Astronomy* (Springer-Verlag, New York, 2003).
 - [130] E. E. Flanagan and T. Hinderer, Transient resonances in the inspirals of point particles into black holes, *Phys. Rev. Lett.* **109**, 071102 (2012), arXiv:1009.4923 [gr-qc].
 - [131] U. Ruangsri and S. A. Hughes, Census of transient orbital resonances encountered during binary inspiral, *Phys. Rev. D* **89**, 084036 (2014), arXiv:1307.6483 [gr-qc].
 - [132] C. P. L. Berry, R. H. Cole, P. Cañizares, and J. R. Gair, Importance of transient resonances in extreme-mass-ratio inspirals, *Phys. Rev. D* **94**, 124042 (2016), arXiv:1608.08951 [gr-qc].
 - [133] L. Speri and J. R. Gair, Assessing the impact of transient orbital resonances, *Phys. Rev. D* **103**, 124032 (2021), arXiv:2103.06306 [gr-qc].
 - [134] P. Gupta, L. Speri, B. Bonga, A. J. K. Chua, and T. Tanaka, Modeling transient resonances in extreme-mass-ratio inspirals, *Phys. Rev. D* **106**, 104001 (2022), arXiv:2205.04808 [gr-qc].
 - [135] T. A. Apostolatos, G. Lukes-Gerakopoulos, and G. Contopoulos, How to Observe a Non-Kerr Spacetime Using Gravitational Waves, *Phys. Rev. Lett.* **103**, 111101 (2009), arXiv:0906.0093 [gr-qc].
 - [136] G. Lukes-Gerakopoulos, T. A. Apostolatos, and G. Contopoulos, Observable signature of a background deviating from the Kerr metric, *Phys. Rev. D* **81**, 124005 (2010), arXiv:1003.3120 [gr-qc].
 - [137] K. Destounis, A. G. Suvorov, and K. D. Kokkotas, Gravitational-wave glitches in chaotic extreme-mass-ratio inspirals, *Phys. Rev. Lett.* **126**, 141102 (2021), arXiv:2103.05643 [gr-qc].
 - [138] K. Destounis and K. D. Kokkotas, Gravitational-wave glitches: Resonant islands and frequency jumps in non-integrable extreme-mass-ratio inspirals, *Phys. Rev. D* **104**, 064023 (2021), arXiv:2108.02782 [gr-qc].
 - [139] K. Destounis, A. G. Suvorov, and K. D. Kokkotas, Testing spacetime symmetry through gravitational waves from extreme-mass-ratio inspirals, *Phys. Rev. D* **102**, 064041 (2020), arXiv:2009.00028 [gr-qc].
 - [140] A. Eleni, K. Destounis, T. A. Apostolatos, and K. D. Kokkotas, Resonant excitation of eccentricity in spherical extreme-mass-ratio inspirals, *Phys. Rev. D* **110**, 124004 (2024), arXiv:2408.02004 [gr-qc].
 - [141] C.-Y. Chen, F.-L. Lin, and A. Patel, Resonant islands of effective-one-body dynamics, *Phys. Rev. D* **106**, 084064 (2022), arXiv:2206.10966 [gr-qc].
 - [142] G. Contopoulos, G. Lukes-Gerakopoulos, and T. A. Apostolatos, Orbits in a non-Kerr Dynamical System, *Int. J. Bifurc. Chaos* **21**, 2261 (2011), arXiv:1108.5057 [gr-qc].
 - [143] G. Lukes-Gerakopoulos and V. Witzany, Non-linear effects in EMRI dynamics and their imprints on gravitational waves 10.1007/978-981-15-4702-7-42-1 (2021), arXiv:2103.06724 [gr-qc].
 - [144] K. Destounis, G. Huez, and K. D. Kokkotas, Geodesics and gravitational waves in chaotic extreme-mass-ratio inspirals: The curious case of Zipoy-Voorhees black-hole mimickers (2023), arXiv:2301.11483 [gr-qc].
 - [145] K. Destounis, F. Angeloni, M. Vaglio, and P. Pani, Extreme-mass-ratio inspirals into rotating boson stars: Nonintegrability, chaos, and transient resonances, *Phys. Rev. D* **108**, 084062 (2023), arXiv:2305.05691 [gr-qc].
 - [146] C.-Y. Chen, H.-W. Chiang, and A. Patel, Resonant orbits of rotating black holes beyond circularity: Discontinuity along a parameter shift, *Phys. Rev. D* **108**, 064016 (2023), arXiv:2306.08356 [gr-qc].
 - [147] S. Mukherjee, O. Kopacek, and G. Lukes-Gerakopoulos, Resonance crossing of a charged body in a magnetized Kerr background: an analogue of extreme mass ratio inspiral (2022), arXiv:2206.10302 [gr-qc].
 - [148] A. Eleni and T. A. Apostolatos, Enhanced plateau effect at resonance in realistic nonintegrable extreme-mass-ratio inspirals, *Phys. Rev. D* **108**, 124044 (2023), arXiv:2306.17762 [gr-qc].
 - [149] W. M. Vieira and P. S. Letelier, Chaos around a Henon-Heiles inspired exact perturbation of a black hole, *Phys. Rev. Lett.* **76**, 1409 (1996), arXiv:gr-qc/9604037.
 - [150] A. P. S. de Moura and P. S. Letelier, Chaos and fractals in geodesic motions around a nonrotating black hole with an external halo, *Phys. Rev. E* **61**, 6506 (2000), arXiv:chao-dyn/9910035.
 - [151] C. M. Will, Perturbation of a Slowly Rotating Black Hole by a Stationary Axisymmetric Ring of Matter. I. Equilibrium Configurations, *Astrophys. J.* **191**, 521 (1974).
 - [152] J. P. S. Lemos and P. S. Letelier, Exact general relativistic thin disks around black holes, *Phys. Rev. D* **49**, 5135 (1994).
 - [153] P. Kotlařík and D. Kofroň, Black Hole Encircled by a Thin Disk: Fully Relativistic Solution*, *Astrophys. J.* **941**, 25 (2022), arXiv:2211.04823 [gr-qc].
 - [154] A. Einstein, On a stationary system with spherical symmetry consisting of many gravitating masses, *Annals Math.* **40**, 922 (1939).
 - [155] P. A. Hogan, A reconstruction in Minkowskian spacetime of Einstein's assembly of test particles, *General Relativity and Gravitation* **9**, 1021 (1978).
 - [156] H. S. Zepolsky, Can the Redshifts of Quasi-Stellar Objects BE Gravitational?, *The Astrophysical Journal Letters* **153**, L163 (1968).
 - [157] P. S. Florides, A New Interior Schwarzschild Solution, *Proceedings of the Royal Society of London Series A* **337**, 529 (1974).
 - [158] G. L. Comer and J. Katz, Thick Einstein shells and their mechanical stability, *Class. Quant. Grav.* **10**, 1751

- (1993).
- [159] B. Kumar Datta, Non-static spherically symmetric clusters of particles in general relativity: I, *General Relativity and Gravitation* **1**, 19 (1970).
 - [160] H. Bondi, On datta's spherically symmetric systems in general relativity, *General Relativity and Gravitation* **2**, 321 (1971).
 - [161] J. R. Gair, Spherical universes with anisotropic pressure, *Class. Quant. Grav.* **18**, 4897 (2001), [arXiv:gr-qc/0110017](#).
 - [162] S. J. Szybka and M. Rutkowski, Einstein clusters as models of inhomogeneous spacetimes, *Eur. Phys. J. C* **80**, 397 (2020), [arXiv:1812.11112 \[gr-qc\]](#).
 - [163] A. Mahajan, T. Harada, P. S. Joshi, and K.-i. Nakao, Critical Collapse of Einstein Cluster, *Prog. Theor. Phys.* **118**, 865 (2007), [arXiv:0710.4315 \[gr-qc\]](#).
 - [164] G. Magli, Gravitational collapse with nonvanishing tangential stresses. 2. Extension to the charged case and general solution, *Class. Quant. Grav.* **15**, 3215 (1998), [arXiv:gr-qc/9711082](#).
 - [165] R. Acharyya, P. Banerjee, and S. Kar, Modelling Einstein cluster using Einasto profile, *JCAP* **04**, 070, [arXiv:2311.18622 \[gr-qc\]](#).
 - [166] C. G. Boehmer and T. Harko, On Einstein clusters as galactic dark matter halos, *Mon. Not. Roy. Astron. Soc.* **379**, 393 (2007), [arXiv:0705.1756 \[gr-qc\]](#).
 - [167] K. Lake, Galactic halos are Einstein clusters of WIMPs (2006), [arXiv:gr-qc/0607057](#).
 - [168] A. Geralico, F. Pompei, and R. Ruffini, On Einstein clusters, *Int. J. Mod. Phys. Conf. Ser.* **12**, 146 (2012).
 - [169] P. G. S. Fernandes and V. Cardoso, Dark matter as a vector field: an action principle for the Einstein cluster (2025), [arXiv:2505.00563 \[gr-qc\]](#).
 - [170] I. King, The structure of star clusters. I. An Empirical density law, *Astron. J.* **67**, 471 (1962).
 - [171] W. Jaffe, A simple model for the distribution of light in spherical galaxies, *Monthly Notices of the Royal Astronomical Society* **202**, 995 (1983), <https://academic.oup.com/mnras/article-pdf/202/4/995/18194452/mnras202-0995.pdf>.
 - [172] J. F. Navarro, C. S. Frenk, and S. D. M. White, The Structure of cold dark matter halos, *Astrophys. J.* **462**, 563 (1996), [arXiv:astro-ph/9508025](#).
 - [173] H. Zhao, Analytical models for galactic nuclei, *Mon. Not. Roy. Astron. Soc.* **278**, 488 (1996), [arXiv:astro-ph/9509122](#).
 - [174] P. G. S. Fernandes and V. Cardoso, <https://github.com/pgsfernandes/SpinningGalacticBlackHoles>, see also <https://the-center-of-gravity.com/data-and-routines/>.
 - [175] P. G. S. Fernandes and D. J. Mulryne, A new approach and code for spinning black holes in modified gravity, *Class. Quant. Grav.* **40**, 165001 (2023), [arXiv:2212.07293 \[gr-qc\]](#).
 - [176] R. H. Boyer and R. W. Lindquist, Maximal analytic extension of the Kerr metric, *J. Math. Phys.* **8**, 265 (1967).
 - [177] C. W. Misner, K. S. Thorne, and J. A. Wheeler, *Gravitation* (W. H. Freeman, San Francisco, 1973).
 - [178] P. Kocherlakota and R. Narayan, Doubly Separable Spacetimes and Symmetry Constraints on their Self-Gravitating Matter Content (2025), [arXiv:2507.18706 \[gr-qc\]](#).
 - [179] P. Lynch, V. Witzany, M. van de Meent, and N. Warburton, Fast inspirals and the treatment of orbital resonances, *Class. Quant. Grav.* **41**, 225002 (2024), [arXiv:2405.21072 \[gr-qc\]](#).
 - [180] E. Levati, A. Cárdenas-Avendaño, K. Destounis, and P. Pani, Cumulative effect of orbital resonances in extreme-mass-ratio inspirals, *Phys. Rev. D* **111**, 104006 (2025), [arXiv:2502.20457 \[gr-qc\]](#).
 - [181] J. Möser, On invariant curves of area-preserving mappings of an annulus, *Nachr. Akad. Wiss. Göttingen, II*, 1 (1962).
 - [182] V. I. Arnol'd, Proof of a theorem of a. n. kolmogorov on the invariance of quasi-periodic motions under small perturbations of the hamiltonian, *Russian Mathematical Surveys* **18**, 9 (1963).
 - [183] G. D. Birkhoff, Proof of poincaré's geometric theorem, *Transactions of the American Mathematical Society* **14**, 14 (1913).
 - [184] L. Barack, Gravitational self force in extreme mass-ratio inspirals, *Class. Quant. Grav.* **26**, 213001 (2009), [arXiv:0908.1664 \[gr-qc\]](#).
 - [185] G. Lukes-Gerakopoulos, Adjusting chaotic indicators to curved spacetimes, *Phys. Rev. D* **89**, 043002 (2014), [arXiv:1311.6281 \[gr-qc\]](#).
 - [186] Z. Pan, Z. Lyu, and H. Yang, Mass-gap extreme mass ratio inspirals, *Phys. Rev. D* **105**, 083005 (2022), [arXiv:2112.10237 \[astro-ph.HE\]](#).
 - [187] K. Destounis and K. D. Kokkotas, Slowly-rotating compact objects: the nonintegrability of Hartle–Thorne particle geodesics, *Gen. Rel. Grav.* **55**, 123 (2023), [arXiv:2305.18522 \[gr-qc\]](#).
 - [188] N. J. Cornish and T. B. Littenberg, BayesWave: Bayesian Inference for Gravitational Wave Bursts and Instrument Glitches, *Class. Quant. Grav.* **32**, 135012 (2015), [arXiv:1410.3835 \[gr-qc\]](#).
 - [189] S. B. Coughlin *et al.*, Classifying the unknown: discovering novel gravitational-wave detector glitches using similarity learning, *Phys. Rev. D* **99**, 082002 (2019), [arXiv:1903.04058 \[astro-ph.IM\]](#).
 - [190] M. Cabero *et al.*, Blip glitches in Advanced LIGO data, *Class. Quant. Grav.* **36**, 15 (2019), [arXiv:1901.05093 \[physics.ins-det\]](#).
 - [191] M. C. Edwards, P. Maturana-Russel, R. Meyer, J. Gair, N. Korsakova, and N. Christensen, Identifying and Addressing Nonstationary LISA Noise, *Phys. Rev. D* **102**, 084062 (2020), [arXiv:2004.07515 \[gr-qc\]](#).
 - [192] N. J. Cornish, T. B. Littenberg, B. Bécsy, K. Chatziioannou, J. A. Clark, S. Ghonge, and M. Millhouse, BayesWave analysis pipeline in the era of gravitational wave observations, *Phys. Rev. D* **103**, 044006 (2021), [arXiv:2011.09494 \[gr-qc\]](#).
 - [193] K. Chatziioannou, N. Cornish, M. Wijngaarden, and T. B. Littenberg, Modeling compact binary signals and instrumental glitches in gravitational wave data, *Phys. Rev. D* **103**, 044013 (2021), [arXiv:2101.01200 \[gr-qc\]](#).
 - [194] M. Muratore, J. Gair, O. Hartwig, M. L. Katz, and A. Toubiana, A pipeline for searching and fitting instrumental glitches in LISA data (2025), [arXiv:2505.19870 \[gr-qc\]](#).
 - [195] E. E. Flanagan, S. A. Hughes, and U. Ruangsri, Resonantly enhanced and diminished strong-field gravitational-wave fluxes, *Phys. Rev. D* **89**, 084028 (2014), [arXiv:1208.3906 \[gr-qc\]](#).
 - [196] Z. Pan, H. Yang, L. Bernard, and B. Bonga, Resonant dynamics of extreme mass-ratio inspirals in a perturbed Kerr spacetime, *Phys. Rev. D* **108**, 104026

(2023), [arXiv:2306.06576](#) [gr-qc].